Research paper

Efficient adsorption of iodide from water by chrysotile bundles with wedge-shaped nanopores

Wenbin Yu[a,b], Huifang Xu[b,*], Eric E. Roden[b], Quan Wan[a,c]

[a] State Key Laboratory of Ore Deposit Geochemistry, Institute of Geochemistry, Chinese Academy of Sciences, Guiyang, Guizhou 550081, China
[b] Department of Geosciences, University of Wisconsin–Madison, Madison, WI 53706, United States
[c] CAS Center for Excellence in Comparative Planetology, Hefei 230026, China

ABSTRACT

Immobilization of iodide (I^-) from groundwater and soils is a challenging subject due to the large size and low charge of I^-. Clay minerals and (hydr)oxides generally exhibit very low adsorption capacity due to anion exclusion or weak attraction. For the first time, the adsorption of I^- by chrysotile bundles (Chry-B) was investigated and a characteristic mechanism was established by comparing the adsorption of I^- on Chry-B with dispersed chrysotile single nanotubes, lizardite and brucite. The adsorption of I^- by Chry-B reached equilibrium with 24 h, and Chry-B exhibited very strong adsorption to I^-, with a distribution coefficient (K_d) of 179.24 mL/g, which is two orders of magnitude higher than those for previously reported clay minerals. The Langmuir adsorption capacity of Chry-B was 4.13 mg/g. The wedge-shaped nanopores among the neighboring nanotubes in Chry-B proved to be the primary adsorption sites for I^-. The I^- at end of the wedge sites was strongly bonded by the nanopores due to the severe superposition of electric potentials from the charged walls of the narrowing wedges. These results demonstrated that chrysotile bundles were a promising candidate for adsorption of I^-, and that the shape of nanopore geometry was crucial in I^- adsorption.

1. Introduction

Radioactive iodines are the by-products of uranium fission, and they are abundant in nuclear wastes (Kaplan et al., 2014; Brix et al., 2019). Radioiodines have been released into soils and the atmosphere during the course of nuclear weapon tests, nuclear power plant operations, and nuclear accidents such as those occurred at Three Mile Island in the USA in 1979, at Chernobyl in Russia in 1986, and at Fukushima in Japan in 2011. The Fukushima Daiichi accident introduced 1.5×10^7 kg ^{131}I to the environment (Von Hippel, 2011), and after the accident, ^{131}I was detected in drinking water in 15 out of the total 47 prefectures in Japan with the highest concentration of 1000 Bq/kg-water in a village of Fukushima, which is > 3 times higher than the radioactive iodine index level for the restriction on drinking water intake in emergency by Nuclear Safety Commission of Japan (Ikari et al., 2015). Radioiodines are especially problematic in groundwater at radiological waste disposal sites, for example, the Hanford Site and the Savannah River Site (Kaplan et al., 2014). Besides, radioactive iodine (such as ^{123}I) is incessantly used in medical treatment and diagnoses (Schoelwer et al., 2015), which add them to hospital wastewater.

Health risk associated with the radioiodine, especially ^{129}I, is a significant environmental concern because of its long half-life (16 million years). It is well known that exposure to even small amounts of radioactive iodines can lead to an increase in metabolic disorders, mental retardation, and thyroid cancer in humans (Choung et al., 2013).

In aqueous environments, iodine exists primarily as the anions iodide (I^-) and iodate (IO_3^-) depending on redox conditions and pH (Um et al., 2004). Of these two species, the reduced form, I^-, is more common in suboxic to reducing conditions with pH values around 4–10 in natural environment (Fuge, 2013). Many efforts have been centered on the application of materials to capture I^- from waste water. Different adsorbents, such as porous carbon (Qian et al., 2008), anion exchange resins (Decamp and Happel, 2013), and Ag, Au or Cu(I) compounds (Yang et al., 2011; Liu et al., 2016; Mushtaq et al., 2017; Chen et al., 2018) were studied for the adsorption of I^- from iodide-bearing water. In a recent paper, the removal of iodine and other radionuclides by novel nanomaterials was critically reviewed (Wang et al., 2019a). Among these, the Ag-based adsorbents are very attractive because of the very strong chemical interaction between I^- and silver
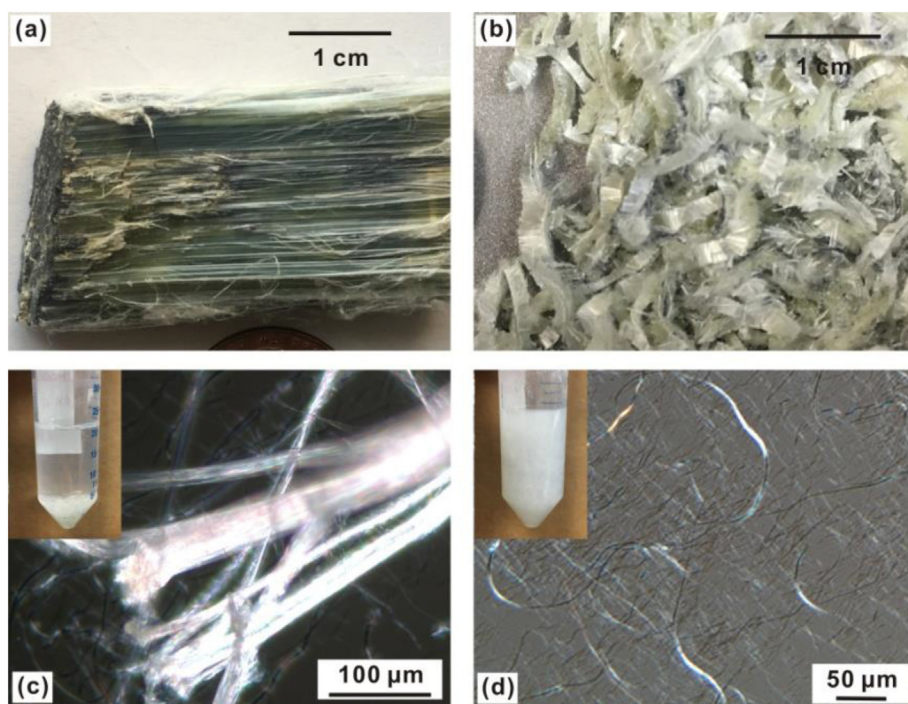
Fig. 1. Photographs and microscopic images of the studied chrysotile samples: (a) chrysotile block, (b–c) chrysotile bundles (Chry-B), and (d) dispersed chrysotile dominated by single nanotubes (Chry-SNT). Insets are the Chry-B and Chry-SNT in the KI solution; Chry-B is sunk at the bottom (c), and the Chry-SNT is uniformly dispersed in the suspension (d).

(Yang et al., 2011; Chen et al., 2018). However, this kind of adsorbents is expensive and unstable (silver leaching occurs under acidic condition), which greatly limits their applications in iodide adsorption.

Natural minerals may be potential adsorbents due to their superior stability and inexpensive availability. A wide variety of minerals have been examined for I^- adsorption, however, most minerals showed little or no I^- adsorption. Miller et al. (2015) measured I^- distribution coefficients (K_d's) for 7 clay minerals including: kaolinite, ripidolite, illite, montmorillonite, palygorskite, sepiolite, and a 70/30 illite/smectite mixed layer, and found the highest K_d value is 1.61 ± 0.28 mL/g for kaolinite. Ticknor and Cho (1990) reported no detectable I^- adsorption on 9 granitic fracture-filling minerals: calcite, quartz, goethite, hematite, chlorite, kaolinite, gypsum, muscovite and epidote. Ticknor et al. (1996) reported low I^- K_d values for biotite (0.7 mL/g) and montmorillonite (1.9 mL/g). Sazarashi et al. (1994) reported no I^- adsorption to montmorillonite ($K_d = 0$ mL/g), low I^- adsorption to allophone ($K_d = 0.726$ mL/g) and attapulgite ($K_d = 0.877$ mL/g), and a relatively high I^- adsorption to cinnabar, likely due to cinnabar contain metal ions which can form iodide compounds with low solubility. Kaplan et al. (2000) reported an appreciable amount of I^- adsorbed to illite (15.14 ± 2.84 mL/g), however, the reason for illite adsorption is unclear and unexplained.

One reason for the low adsorption capacity of the aforementioned minerals to I^- was that the negative surface charge under the experimental conditions tends to repel the anionic I^-. However, some oxides or hydroxides, such as Al-oxide (Muramatsu et al., 1990) or Fe-oxides (Couture and Seitz, 1983) carrying positive charges at the experimental conditions, still showed very low I^- adsorption. Yu et al. (1996) compared the adsorption of I^- by ferrihydrite and imogolite with other common anions, such as chloride, perchlorate, and phosphate, and they found that the amount of I^- adsorption was about 1% of other anions' capability. Another reason for the low I^- adsorption is probably due to its large size and atomic weight. The size and atomic weight of I^- are 1.2 and 3.6 times larger than those of chloride, respectively (Baxter and Titus, 1940). The large size increases the interaction distance and further weakens the attraction between the ion and adsorbent surface. So it is challenging to capture I^- from aqueous solutions due to its weak adsorption tendency. Therefore, it is important to find a new adsorbent for I^- adsorption and understand its adsorption mechanism.

Chrysotile is a tubular or fibrous hydrated magnesium silicate belonging to the serpentine group. Its idealized chemical formula is $Mg_3Si_2O_5(OH)_4$. Structurally all the serpentine group minerals contain a tetrahedral sheet and a brucite-like octahedral sheet (Wicks and Plant, 1979). The structure misfit between the sheet (lateral dimension of the tetrahedral sheet is smaller than that of the octahedral sheet) causes a curvature and formation of the nanotube-shaped morphology of chrysotile. The individual chrysotile nanotubes were reported to have apparent outer diameters in the range of 10 to 50 nm and inner diameters in the range of 1 to 10 nm (Sprynskyy et al., 2011). Natural chrysotile usually occurred in the form of bundles, and the pores among the neighboring nanotubes have an effective pore size of the same order of magnitude as the internal pores of the nanotubes (Pundsack, 1961). Chrysotile has many unique physical and chemical characteristics, such as incombustibility, chemical stability, physical durability, and mechanical flexibility (Wang et al., 2019b). Consequently, chrysotile has been wildly used in numerous industrial applications, for example, thermal insulation materials, filtering devices and friction material for brakes (Pye, 1979). In particular, chrysotile shows good adsorption properties for some anionic species (Valentim and Joekes, 2006). This is related to chrysotile with positively charged outer surface in the pH range of 2–10 due to its point of zero charge (PZC) at pH of 10.8–11.0 (Stumm, 1992; Pokrovsky and Schott, 2004). However, there is currently no report on the adsorption of I^- by chrysotile.

In the present work, chrysotile, both in the form of bundles and dispersed single nanotubes, were used for I^- adsorption experiments. Lizardite, the serpentine group mineral with flat tetrahedral and octahedral sheet, and brucite, with a lattice configuration that is similar to the Mg-bearing octahedral layers in serpentine minerals, were also studied for comparison purposes. A characteristic mechanism of I^- interaction with chrysotile bundles was established. The fundamental information derived from this study is important for the potential use of chrysotile in I^- adsorption and development of new efficient anion adsorbents in future.

2. Materials and methods

2.1. Chemicals and materials

Non-radioactive iodine (^{127}I) was used in I^- uptake experiments. Crystalline potassium iodide (KI) (Fisher Scientific Co., USA) was used as the source of I^-. $MgSO_4$ (AR Grade), NaOH (AR Grade) and 36.7% HCl were purchased from Fisher Scientific. Deionized water (resistivity, 18.2 MΩ·cm) was used in all of the experiments. All chemicals were used as received, without further purification.

The raw chrysotile was from Quebec, Canada, and the sample was cut from the centers of a chrysotile vein to avoid contamination with minerals from the wall rock. An intact block of chrysotile is shown in Fig. 1a. The chrysotile block was torn into small pieces with a tweezer, and then cut into approximately 2 mm length with a scissor, to produce the chrysotile bundles (Fig. 1b and c). The obtained chrysotile bundles were denoted as Chry-B. Mechanically grinding and dispersion of Chry-B was carried out in the following steps: Chry-B was placed in an agate mortar and ground for 1 h in an absolute ethanol, and then the ground sample was placed in ethanol and stirred with a magnetic stirrer for 3 h. After that, the solid phase in the mixture was filtered and dried. The dried sample was then placed in a beaker containing distilled water, dispersed by an ultrasonic shaker for 1 h so that the nanotubes in the bundles were dispersed as much as possible. Then the ultrasonicated samples were filtered and dried, to produce well-dispersed chrysotile single nanotubes (Fig. 1d), which were designated by Chry-SNT.

Lizardite was from Del Puerto Ophiolite nearby Paterson of California, USA (Evarts, 1977). Brucite was synthesized through addition of a saturated $MgSO_4$ solution to a constantly stirred 1 mol/L (M) NaOH solution (Li et al., 2014).

2.2. Characterization

X-ray diffraction (XRD) data were collected on a Rigaku Rapid II instrument (Mo $K\alpha$ radiation) with a two-dimensional (2D) image-plate detector in the Department of Geosciences at the University of Wisconsin–Madison. All the XRD patterns were collected at 50 kV and 50 mA using a 100-μm diameter beam collimator. The conventional 2θ vs. intensity patterns were produced by converting the 2D images using the Rigaku's 2DP software.

The low-temperature nitrogen (N_2) adsorption-desorption isotherms were measured using an Autosorb-iQ2-MP gas adsorption analyzer (Quantachrome, Boynton Beach, FL) at liquid-nitrogen temperature. Before measurement, the samples were outgassed at 200 or 150 °C (200 °C for Chry-B and Chry-SNT, 150 °C for lizardite and brucite) for 12 h under vacuum. The total specific surface area of the sample, S_{BET}, was calculated from the nitrogen adsorption data using the multiple-point Brunauer-Emmett-Teller (BET) method, and the total pore volume, V_{total}, was evaluated based on N_2 uptake at a relative pressure of approximately 0.99. The pore size distribution curves, nanoporosity and pore specific surface area were derived from the nonlocal density functional theory (NLDFT) model (NLDFT-N_2-silica at 77 k, based on a cylindrical pore model).

TEM images were obtained using a Philips CM200-UT microscope operated at an accelerating of 200 kV in the Materials Science Center at the University of Wisconsin–Madison. The specimens were prepared by the following procedure: the Chry-B and Chry-SNT samples were ultrasonically dispersed in ethanol for 5 min, and a droplet of the sample suspension was then dropped onto a lacy carbon-coated 200-mesh Cu grid which was left to stand for at least 10 min before being transferred into the microscope.

2.3. Iodide adsorption and desorption experiments

Batch experiments of I^- adsorption were carried out by shaking 0.1 g dry samples with 20 mL of I^- solutions in a 50 mL centrifuge tube

fitted with a cap at 25 °C. The I^- solution was prepared by dissolving KI in deionized water. The initial pH and final pH were measured using a pH meter (Accumet XL20, Fisher Scientific). For the kinetics tests, the initial concentration of I^- in the solution was 0.25 mmol/L (mM), and the mixture in the centrifuge tubes was strongly shaken at a rate of 150 rpm in a platform shaker. The adsorption time was in the range from 1 to 48 h. At the end of each time intervals, the suspensions were centrifuged at 4000 rpm for 10 min, and then the supernatants were removed with a pipette and refrigerated for I^- concentrations analysis. A Dionex 1000 Ion Chromatography (IC) with an AS22 guard and analytical column was used to measure I^- concentrations, with a 5.4 mM Na_2CO_3/1.68 mM $NaHCO_3$ solution as the eluent.

The experiments for the comparison adsorption of the four samples (Chry-B, Chry-SNT, lizardite, and brucite) followed a very similar procedure with the kinetics experiments except for the shaken time is 48 h as determined from the kinetics experiment (see following). A Chry-B/pH adsorption experiment was conducted to determine the effect of pH on the adsorption of I^- by Chry-B. The pH values of the suspensions were adjusted approximately to 5.0, 7.0, 8.0, and 9.0, respectively by incrementally adding 0.1 M NaOH or 0.1 M HCl. The NaOH and HCl were added every 12 h until the desired pH was obtained and did not change > 0.1 pH units during a 48 h period. The experiments performed to obtain the adsorption isotherm also followed a very similar procedure, and the initial concentrations of I^- in the solutions were 0, 0.05, 0.1, 0.2, 0.5, and 1 mM, respectively. Each adsorption point was the average of duplicate or triplicate experiments. Blank experiments confirmed the absence of wall adsorption or I^- loss to volatilization.

Solid: liquid partitioning coefficients (K_d values, mL/g) were calculated using the following equation:

$$K_d = (C_0 - C_t)/(C_t \times S) \tag{1}$$

where C_0 and C_t (mmol/L, mM) are the concentration of I^- in the reaction solution before and after adsorption for time t (h), respectively. S is the solid:solution ratio (g/mL). The amount of I^- adsorbed per unit mass of the adsorbent at time t (h), q_t (mg/g) was calculated as:

$$q_t = (C_0 - C_t) \times M/m \tag{2}$$

where M is the molar mass of I^-, and m (g) is the amount of adsorbent in 1 L of I^- solution.

After adsorption experiments, the solid samples were collected by centrifugation and sequentially used to conduct the desorption experiments. The solid samples with adsorbed I^- were sequentially exposed to 20 mL deionized water, shaking on a platform shaker (150 rpm) for 1 to 48 h. At the end of each time intervals, the suspensions were centrifuged and the supernatants were used to determine the I^- concentration using the same method as in the adsorption experiments. The amounts of I^- desorbed from each samples were then calculated based on the concentration of I^- in the desorption solutions, $C_{d(t)}$ (mM). The desorption mass percentage (%) was calculated using the equation:

$$Desorption\ (\%) = [C_{d(t)}/(C_0 - C_F)] \times 100 \tag{3}$$

where, C_F (mM) is the concentration of I^- in the reaction solution after adsorption.

3. Results and discussion

3.1. Characterization of samples

The XRD patterns of the raw chrysotile, lizardite and brucite are illustrated in Fig. 2. The reflection positions of the raw chrysotile match those reported on an ICDD PDF No.00-043-0662 (Fig. 2), indicating the raw chrysotile is a clino-chrysotile. The monoclinic nature of the raw chrysotile is also indicated by the 20 l reflection, particularly the 202 reflection at 2.452 Å and the 202(_) reflection at 2.543 Å (Bailey, 1988). The XRD pattern of the raw chrysotile did not contain any diffraction for other minerals (Fig. 2a), indicating the raw chrysotile sample was
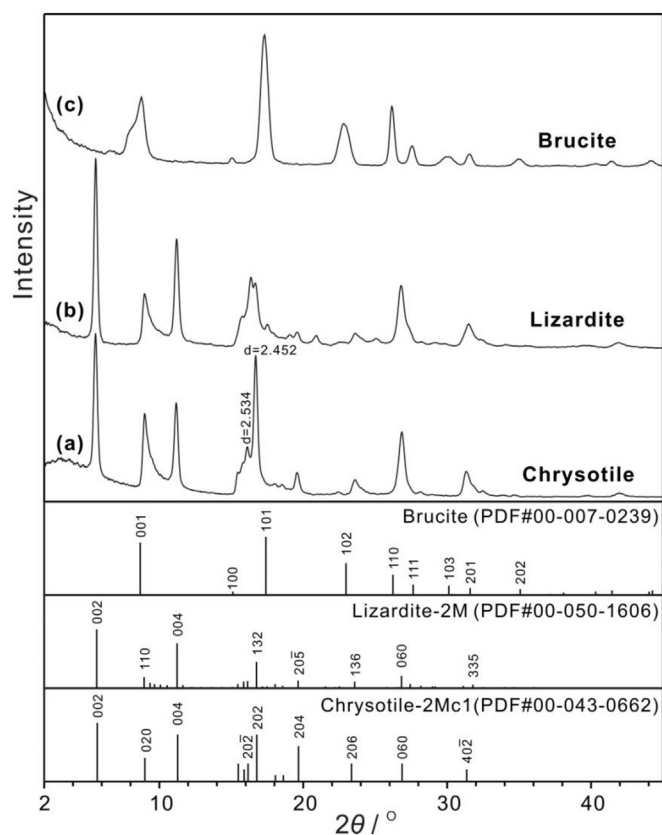
Fig. 2. XRD patterns of the (a) raw chrysotile, (b) lizardite and (c) synthetic brucite.

relatively pure. It can be seen from the XRD pattern from lizardite (Fig. 2b) that is dominated by lizardite-2M polytype. The most intense reflection of lizardite-2M occur at the *d*-values of 7.3 Å and 3.65 Å, attributed to the 002 and 004 reflection of lizardite-2M. The synthetic brucite shows broad XRD reflection (Fig. 2c), indicating the nanosized particles and a poorly-ordered nature of the synthetic brucite. The 001 reflection of the brucite exhibits asymmetry, with a shoulder at the low angle side. This result reflects that the sheet of the synthetic brucite is pseudo-hexagonal due to local distortion and poorly ordered structure. A similar XRD pattern of brucite synthesized by MgO hydrolysis in weak acid at the initial stage was reported by Li et al. (2014).

The chrysotile block exhibits characteristic pale green color (Fig. 1a), but when it was cut into small bundles, it becomes lighter (Fig. 1b). Single chrysotile nanotubes were reported to have a white color (Pasbakhsh and Churchman, 2015). The optical photomicrograph illustrated the bundles of chrysotile from 10 to 50 μm in size (Fig. 1c). TEM images from the dispersed chrysotile show thinner bundles and dispersed nanotubes (Fig. 3a–c). The outer diameter of the individual nanotubes shows a great variation, with a range of 15–40 nm (Fig. 3b). The chrysotile nanotubes have a cylindrical shape (Fig. 3c), indicating that the nanotubes are hollow. The diameter of the internal pores within the nanotubes ranges from 3 to 4 nm as observed from the TEM images. Fig. 3c shows a chrysotile nanotube with an internal pore diameter of 3.8 nm, and its fast Fourier transform (FFT) pattern shows the characteristic lines of streaking that are marked by arrows (Cattaneo et al., 2012). As natural chrysotile usually occurred in the form of bundles (Figs. 1c and 3a), the special wedge-shaped nanopores were formed in the packing space among the neighboring nanotubes in the bundles (Fig. 3d). Porosity data calculated from the N_2 adsorption isotherms, which are of more statistical significance, are given below.

The reason why natural chrysotile occurred in the form of bundles is complex. Martin and Phillips (1977) reported that the hydrogen

bonding and Van der Waal's bonding are likely to be the main inter-tubes binding mechanisms. From a recently reported high-resolution TEM image of the cross-section of chrysotile prepared by a new method of ion slicing (Fig. S1, see the Supporting Information), it shows the bonding between nanotube surface and edge layers from the adjacent nanotubes (Fig. S1-A), and a continuous layer between two adjacent nanotubes (Fig. S1-B) (Ohnishi et al., 2010). So we believe that chemical bonds exist between the neighboring nanotubes. The possible bonding patterns of the chemical bonds are schematically illustrated in the right panels of Fig. S1. Ji et al. (2018) also found the 1:1 type serpentine minerals can be transformed into 2:1 type smectite via dissolution of Mg-octahedral sheets and the inversed tetrahedral sheets chemically bonded to the adjacent octahedral sheets. Because the area of contact between adjacent nanotubes is limited (Fig. 3d and Fig. S1), the resultant inter-tubes binding force is weak. This weak binding force can also be manifested by the fact that the chrysotile bundles can be opened further by mechanical (grinding or ultrasonic (Turci et al., 2012)) or/and chemical (using dispersing reagent such as acetic acid or aluminum chloride) (Yang et al., 2007) dispersion treatments.

Fig. 4 show the low-temperature N_2 adsorption-desorption isotherms and the pore size distribution curves. The isotherms for Chry-B and Chry-SNT can both be classified as type IV with H3 hysteresis loops (Fig. 4A-a and A–c), according to the IUPAC classification (Gregg et al., 1982). This type of isotherm is a typical characteristic of mesoporous structures. A sharper increase was observed near the low pressure region in the adsorption isotherm of Chry-SNT (Fig. 4A-c) compared with that of Chry-B (Fig. 4A-a), indicating that larger pores or, more likely, liberated nanotubes were contributing to the nitrogen adsorption in Chry-SNT. The larger pores are formed by the randomly stacking of the well-dispersed nanotubes. As shown by Fig. 4A-b and A-d, lizardite and brucite also show type IV isotherms, indicating mesopore existence in the samples.

The pore size distribution of Chry-B is bimodal, with pore populations centered at 3.7 and 4.3 nm (Fig. 4B-e), which are owing to the internal pores within the nanotubes (Fig. 3c) and the wedge-shaped nanopores formed by the packing of the nanotubes in the bundles (Fig. 3d and Fig. S1). As shown by Fig. 4B-g, the pore populations centered at 3.7 nm still exist in Chry-SNT, implying these pores mainly attribute to the internal pores within the nanotubes, which is consistent with the TEM results. But the left boundary of the peak at 3.7 nm in Chry-SNT shows a small shift towards the large pore size side (Fig. 4B-g) compared with the peak at 3.7 nm in Chry-B (Fig. 4B-e). This result indicated that the wedge-shaped nanopores also contributed to the pore populations centered at 3.7 nm in Chry-B (Fig. 4B-e), and that the wedge-shaped nanopores have a more broad pore size range than the internal pores within the nanotubes. It is noteworthy that the size at the very end of the wedge-shaped nanopores will be extremely small, and this small size can not be reflected from the pore size distribution data. This is because an equivalent cylindrical pore (Fig. 3d) was used to calculate the pore size in the pore size distribution analysis. The pore populations centered at 4.8 nm and the insignificant populations in a wide range from 6 to 40 nm (Fig. 4B–g) are ascribed to the void space between the well-dispersed nanotubes in Chry-SNT. The pore size distributions of lizardite and brucite show obvious mesoporous distribution in Fig. 4B-f and B-h, which are formed via packing of lizardite particles and brucite nano-crystals, respectively.

The specific surface area of Chry-B is 16.4 m^2/g (Table 1), which agrees with the literature value for Canadian chrysotile from Quebec (16.7 m^2/g) (Morgan, 1997). Olson et al. (2008) also reported that the specific surface area of naturally occurring chrysotile generally ranges from 10 to 20 m^2/g. After the dispersion treatment, the specific surface area of Chry-SNT increased to 41.6 m^2/g, which is approximately 2.5 times higher than the specific surface area of the chrysotile in the bundle form (Chry-B). This significant increase in the specific surface area was attributed to the liberation of individual nanotubes, indicating Chry-SNT is dominated by single chrysotile nanotubes. The specific
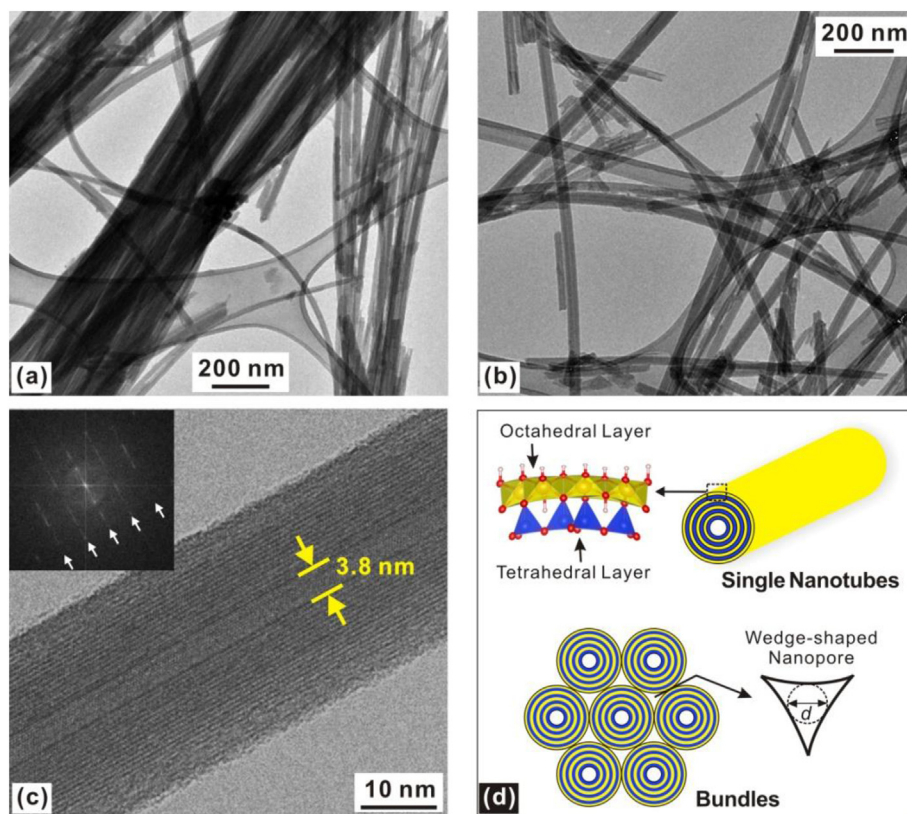
Fig. 3. The structure of chrysotile: (a–c) TEM images of the chrysotile bundles and single nanotubes, inset of Fig. 3c: the fast Fourier transform (FFT) pattern of the single chrysotile nanotube; (d) schematic of single nanotube and "end-on" view of chrysotile bundle following hexagonal closest packing.
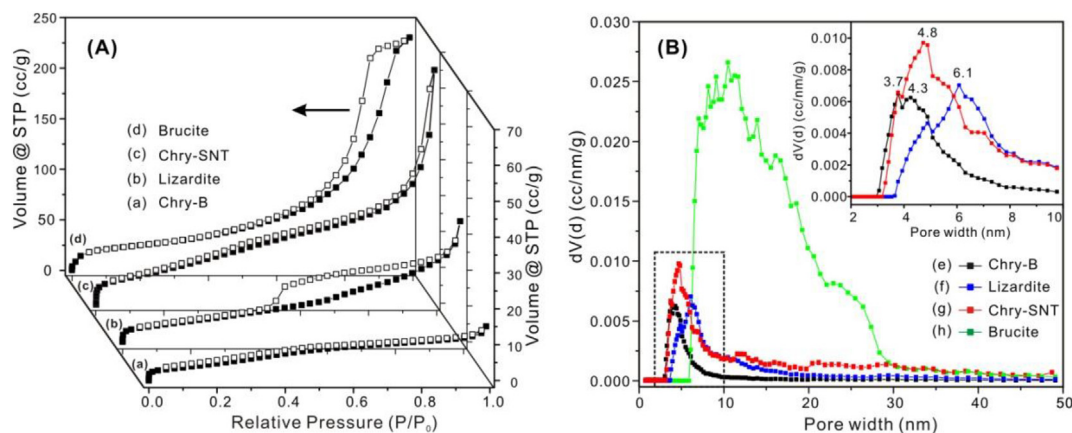

Fig. 4. (A) N_2 adsorption-desorption isotherms and (B) pore size distribution curves of Chry-B, lizardite, Chry-SNT, and brucite.

surface area of Chry-SNT is slightly smaller than that of chemically dispersed chrysotile (50 m^2/g) (Naumann and Dresher, 1966), probably due to incompleted disaggregation of chrysotile bundles and a minor portion of chrysotile nanotubes still existed in the form of bundles. As shown in Table 1, the specific surface area and pore volume of pores < 3.7 nm in Chry-B are larger than those in Chry-SNT, due to more wedge-shaped nanopores existed in Chry-B. The specific surface areas and porous parameters of lizardite and brucite are summarized in

Table 1
Specific surface area values and porous parameters of samples.

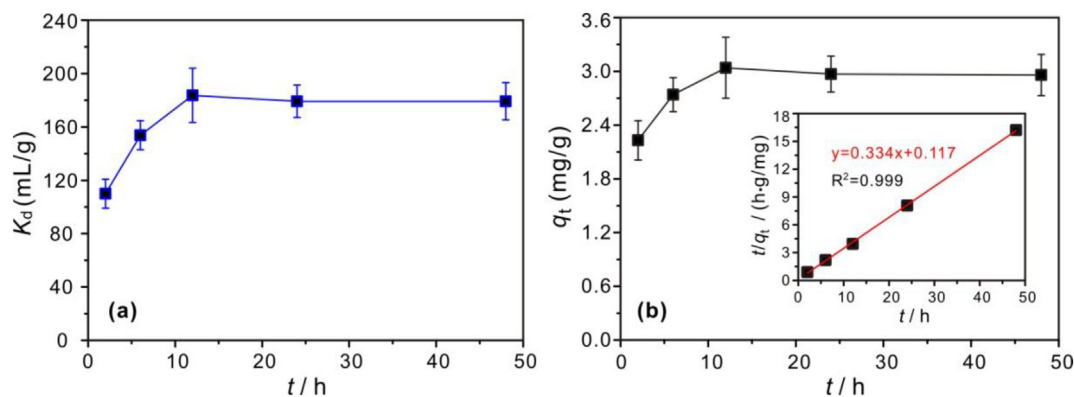| Sample	S_{BET} (m^2/g)	V_{total} (cc/g)	Pore surface area (m^2/g)			Nanoporosity (cc/g)		
			< 3.7 nm	< 6 nm	< 10 nm	< 3.7 nm	< 6 nm	< 10 nm
Chry-B	16.4	0.023	2.7	11.5	13.3	0.0024	0.012	0.016
Chry-SNT	41.6	0.092	1.7	16.1	22.3	0.0015	0.019	0.030
Lizardite	23.2	0.052	0	7.1	14.6	0	0.0088	0.023
Brucite	89.9	0.037	0	0	39.4	0	0	0.080

Fig. 5. (a) Iodide-K_d values as a function of adsorption time and (b) adsorption kinetics of I^- on Chry-B under neutral conditions (inset is the linear fitting plot based on pseudo-second-order kinetic model), pH ≈ 7.

Table 1.

3.2. Performance of samples for iodide adsorption and desorption

To establish the equilibrium time for adsorption and know the kinetics of the adsorption process, I^- adsorption on Chry-B was investigated as a function of adsorption time. As shown in Fig. 5a, the K_d values increase with the adsorption time, and the adsorption of I^- by Chry-B reaches equilibrium within 24 h. The cause for these K_d values increases with adsorption time in the early stage may be attributed to diffusion limitations of the I^- to the adsorption sites. The extended adsorption time would allow I^- to diffuse into the pore structures, thereby permitting I^- to come into contact with additional adsorption sites. From Fig. 4B, we knew that Chry-B had the smallest pore size, so it could be expected that Chry-B would take the longest time to reach the adsorption equilibrium. A period of 48 h was used as the adsorption time for the following experiments to ensure that adsorption equilibrium was reached. The Pseudo-second-order kinetic model demonstrates the optimal one for quantitatively describing the kinetic data for I^- adsorption on Chry-B, compared with several commonly used kinetic models, such as Pseudo-first-order model, Weber and Morris model, and Simplified Elovich model (Largitte and Pasquier, 2016). The linear form of the kinetics curve, t/q_t (h·g/mg) versus t (h) (Fig. 5b), was fitted using the pseudo-second-order rate equation with the following expression (Zhang and Jaroniec, 2017):

$$t/q_t = 1/(kq_e^2) + t/q_e \qquad (4)$$

where q_t (mg/g) is the amount of I^- adsorbed per unit mass of the adsorbent at time t (h), k (g/mg·h) is the pseudo-second-rate constant of adsorption, and q_e (mg/g) is the equilibrium adsorption capacity. The fitting results are shown in Table 2.

The results of the comparison adsorption of the four samples are illustrated in Fig. 6a. The iodide-K_d values for Chry-B, Chry-SNT, lizardite, and brucite are 179.24 ± 13.99, 30.03 ± 14.51, 18.77 ± 15.37, and 2.02 ± 1.55 mL/g, respectively. The K_d value for Chry-B is 6.0 times higher than that for Chry-SNT dominated by single chrysotile nanotubes, and is significantly higher than those for lizardite and brucite (Fig. 6a). As the K_d value is related to the initial concentration of I^-, the previous works with the same or similar initial

Table 2
Kinetics constants and langmuir equation parameters for iodide sorption on chrysotile bundles (Chry-B).

Kinetics constants		Langmuir parameters	
k (g/mg·h)	0.96	b (L/mmol)	18.40
q_e (mg/g)	2.99	Q_m (mg/g)	4.13
R^2	0.999	R^2	0.993

concentrations of I^- was chosen to compare the K_d values with those in this study. The comparison of the K_d for Chry-B with those for 7 clay minerals including: kaolinite, ripidolite, illite, montmorillonite, palygorskite, sepiolite, and a 70/30 illite/smectite mixed layer (with the highest K_d value of 1.61 mL/g for kaolinite) measured by Miller et al. (2015) revealed the K_d for Chry-B is two orders of magnitude higher than those of previously studied clay minerals. This result indicated Chry-B exhibited very strong adsorption to I^-. The K_d value for lizardite is low but seems larger than those for calcite, chlorite, quartz, and vermiculite (all had K_d value < 1 mL/g) (Kaplan et al., 2000). Given the large standard deviation value of the K_d value for lizardite, the ability of I^- adsorption by lizardite may be similar to those by the reported minerals. The K_d value for brucite is also low, similar to the value for goethite (0.4 ± 2.9 mL/g) (Ticknor et al., 1996).

The specific surface area normalized K_d values, K_{d-s} were calculated by normalizing to the specific surface area (Table 1) by dividing the traditional K_d values. As shown in Fig. 6a, the K_{d-s} value of Chry-B remained significantly greater than those of the other three samples. The K_{d-s} value of Chry-B is 10.9 ± 0.85 mL/m², which is 15.6 times larger than that of Chry-SNT (0.7 ± 0.35 mL/m²), indicating the wedge-shaped nanopores in Chry-B enhance the interaction between chrysotile nanotubes and I^-. Both K_{d-s} and K_d results revealed that Chry-B exhibited the strongest adsorption for I^-, and the wedge-shaped nanopores in Chry-B were the primary adsorption site for I^-. The K_d of Chry-SNT is slightly greater than those of other minerals reported in the literature (Ticknor et al., 1996; Kaplan et al., 2000), attributed to incomplete disaggregation and small portion of wedge-shaped nanopores existed in Chry-SNT.

Fig. 6b shows the adsorption isotherms of I^- on Chry-B. The Langmuir adsorption isotherm model demonstrates the best fit for quantitatively describing the adsorption data compared with several commonly used fitting models, such as the Freundlich and Redlich-Peterson models (Limousin et al., 2007). The Langmuir model is described by the following equation (Liu et al., 2012; Yuan et al., 2013):

$$Q_e = Q_m bC_e/(1 + bC_e) \qquad (5)$$

where Q_e (mg/g) is the amount of adsorbed I^- at equilibrium concentration C_e (mM), Q_m (mg/g) and b are the Langmuir adsorption capacity and Langmuir constant, respectively. The adsorption coefficients computed from Eq. (5) are summarized in Table 2. The Langmuir adsorption capacity of Chry-B is 4.13 mg/g (Table 2), which is three orders of magnitude higher than those of natural soil samples (Dai et al., 2009), one order of magnitude higher than that of ferrihydrite (Yu et al., 1996), and around the same order of magnitude of black carbon (Choung et al., 2013). What is more, to the best of our knowledge, the chrysotile bundles (Chry-B) exhibits the greatest adsorption capacity (K_d or q_m value), compared with all the clay minerals even (hydr)oxides reported in the literature (Couture and Seitz, 1983;
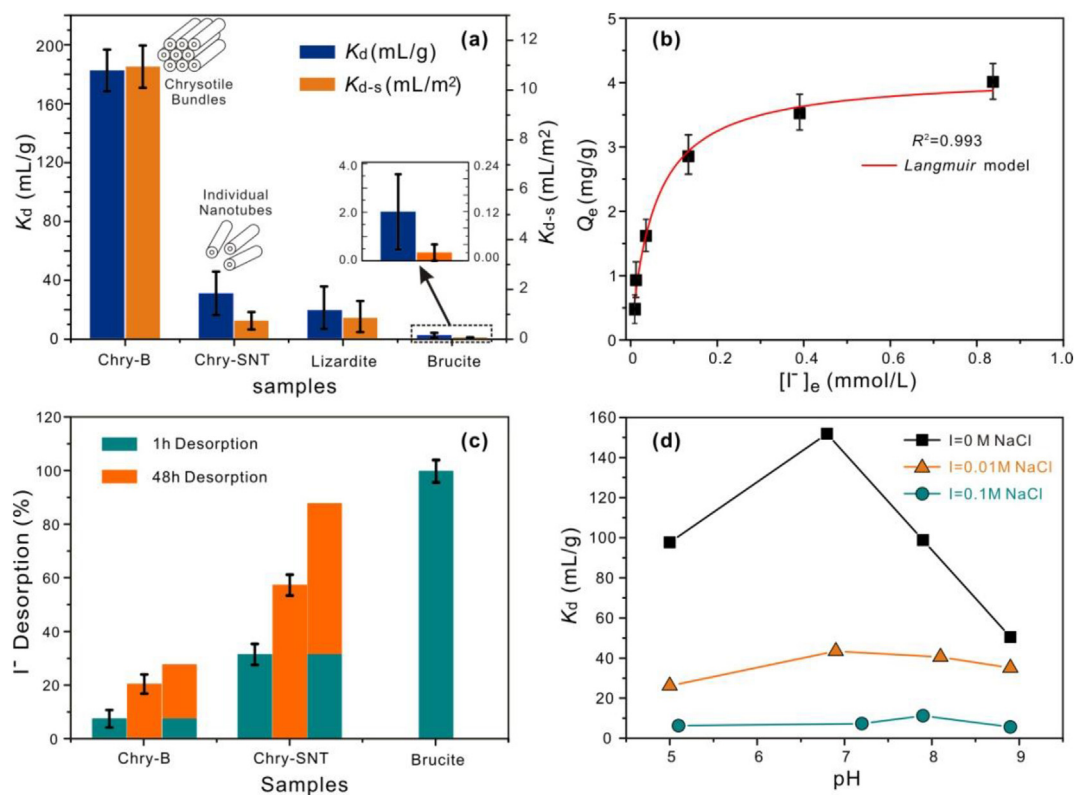
Fig. 6. (a) Iodide-K_d and iodide-K_{d-s} values for different samples under neutral conditions, pH = 7.0 $\pm$ 0.2 (for brucite, pH = 10 was used for the sample stability (Pokrovsky and Schott, 2004)); (b) adsorption isotherm of I$^-$ on Chry-B; (c) percentage of I$^-$ desorption by sequential extraction of pre-adsorbed samples by deionized water for 1 h and 48 h; and (d) effect of pH and ionic strength on the I$^-$ adsorption on Chry-B. Triangles: I = 0.01 M; circles: I = 0.1 M, which are 40 and 400 times higher than the concentration of I$^-$ (0.25 mM) in the solution.

Muramatsu et al., 1990; Ticknor and Cho, 1990; Sazarashi et al., 1994; Ticknor et al., 1996; Yu et al., 1996; Kaplan et al., 2000; Miller et al., 2015).

The results of desorption experiments of pre-adsorbed I$^-$ are shown in Fig. 6c. A minor portion of the pre-adsorbed I$^-$ (6.9%) was desorbed from the Chry-B after exposure to deionized water for 1 h, probably due to the release of weak-bonded I$^-$ on the external surface of Chry-B. In contrast, 31.0% and 100% of pre-adsorbed I$^-$ was mobilized from Chry-SNT and brucite, respectively, after exposure to deionized water for 1 h. Extending the time of desorption of I$^-$ to 48 h resulted in 19.8% more of I$^-$ release, a total of 26.7% of I$^-$ was released from Chry-B, and in contrast, totally 88.8% of the pre-adsorbed I$^-$ was released from Chry-SNT (Fig. 6c). This result indicated that Chry-B exhibited the strongest attraction to I$^-$, compared to Chry-SNT and brucite, the remaining 73.3% of I$^-$ in Chry-B and 11.2% of I$^-$ in Chry-SNT appearing strongly bonded in the wedge-shaped nanopores. These strongly adsorbed iodide anions may be at the very end of the wedge-shaped sites (see following Fig. 7a).

The Chry-B/pH experiment was conducted to evaluate the extent that I$^-$ adsorption to chrysotile bundles was pH dependent. As the pH of the system decreased below 9, the amount of I$^-$ adsorbed to Chry-B increased appreciably (Fig. 6d). Considering that the PZC of chrysotile is higher than pH 10 (Stumm, 1992; Pokrovsky and Schott, 2004), the decreasing pH resulted in a greater extent of protonation of surface hydroxyl groups (coordinated to magnesium, > Mg-OH) and thus more positive charges on the chrysotile surface. The influence of pH on the adsorption capacity suggests that the electrostatic attraction between I$^-$ and > Mg-OH$^+$ surface charges constitutes an important driving force of the adsorption process. At pH approximately 5, a decrease of the amount of I$^-$ adsorption was observed (Fig. 6d), likely due to the removal of positively charged > Mg-OH$^+$ sites in the outer brucite sheet by dissolution and accompanying exposure of underlying > Si-O$^-$

sites on the surface (Bales and Morgan, 1985).

The results of ionic strength dependence experiments showed that pronounced decrease in the adsorption capacity of I$^-$ were observed as the increase of ionic strength (Fig. 6d). A common reason to account for such a depressed adsorption capacity is that an increased ionic strength can lower the electric potential of the charged surface, compress the electric double layer (Wang et al., 2002), and thus weaken the electrostatic attraction between I$^-$ and charged chrysotile surface. Sheppard et al. (1995) reported that Cl$^-$ can compete with I$^-$ in the adsorption process, which may be another reason attributed to the decrease in the adsorption capacity. It is noteworthy that when the concentration of Cl$^-$ is 0.01 M, which is 40 times higher than that of I$^-$ in the solution, the K_d value of Chry-B is as high as 43.48 mL/g (Fig. 6d). This result again indicates that the Chry-B has strong attraction to I$^-$. Based on the perception that out-sphere complexes (compared with inner-sphere complexes) are much susceptible to the introduction of an electrolyte solution during adsorption (Hayes et al., 1987), it can be inferred that out-sphere surface complexation is the dominant mechanism for I$^-$ adsorption on chrysotile bundles.

3.3. Adsorption mechanisms and implications

From the results of adsorption experiments, chrysotile bundles (Chry-B) exhibited the highest adsorption capacity to I$^-$, the electrostatic attraction between I$^-$ and > Mg-OH$^+$ surface charges constitutes an important driving force of the adsorption process, and out-sphere surface complexation is the dominant mechanism for I$^-$ adsorption on Chry-B. However, individual chrysotile nanotubes and brucite with the same surface group (> Mg-OH), and lizardite with flat tetrahedral and octahedral sheets, all show low adsorption capacity to I$^-$ (Fig. 6a). A special mechanism related to the adsorption by the wedge-shaped nanopores in Chry-B was inferred as follows. The wedge-shaped
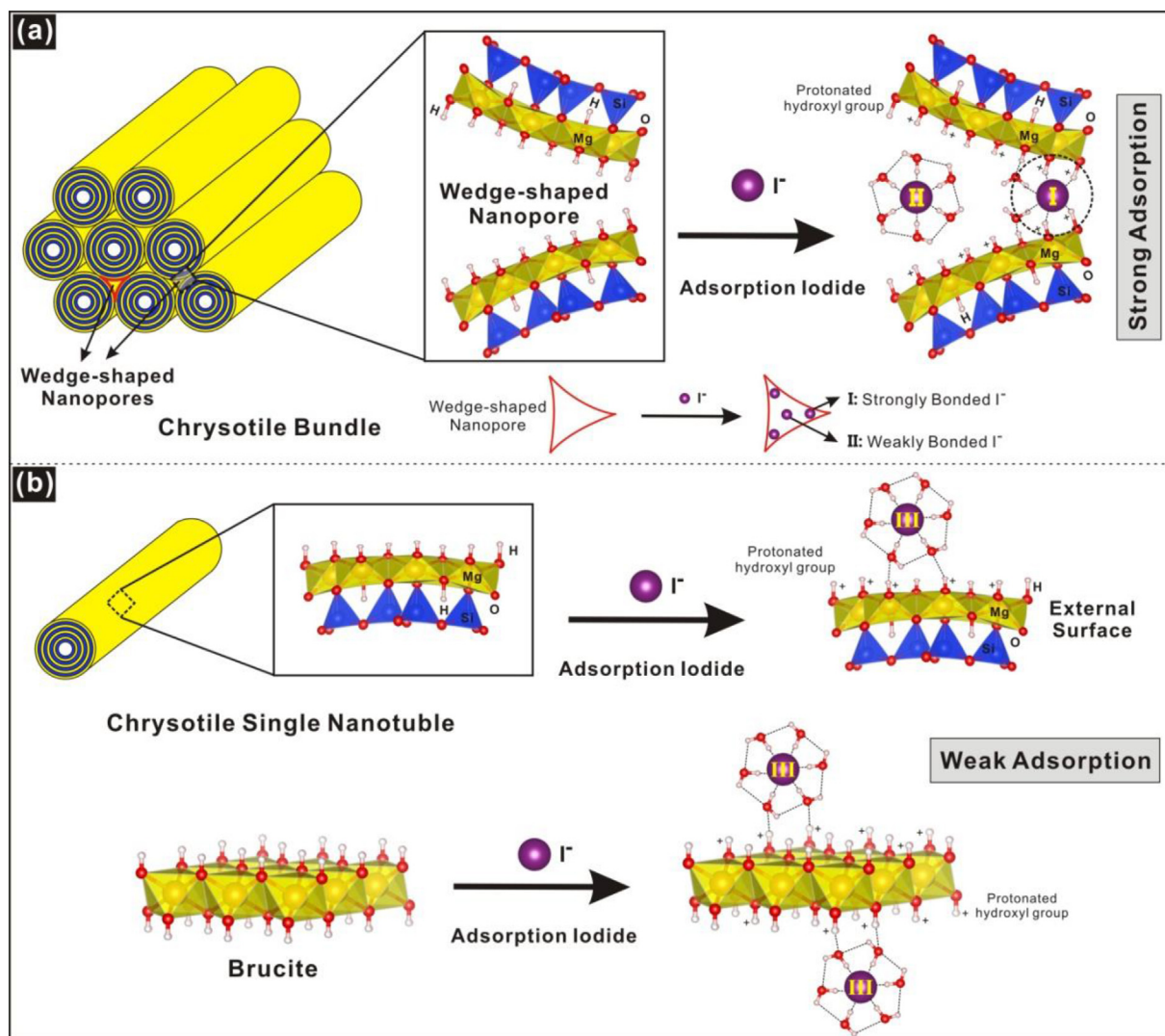
Fig. 7. Schematic presentation for the related mechanism of adsorption of I⁻: (a) on chrysotile bundles; (b) on chrysotile single nanotube and brucite. Labeled I and II are the strong-bonded and weak-bonded I⁻ in the wedge-shaped pores, respectively. The iodide anions with label III are the weakest bonded I⁻ on the external surface of chrysotile single nanotubes or on the flat surfaces of brucite (lizardite with a flat surface of octahedral sheet is similar to brucite).

nanopores in Chry-B are the primary adsorption site for I⁻. As the equivalent diameter of the wedge-shaped nanopores in Chry-B has a broad distribution, with a peak at approximately 4.3 nm (Fig. 4B-e), and the diameter of iodide with an aqueous hydration shell is only approximately 0.72 nm (Küpper et al., 2008), it is easy for the I⁻ to enter the wedge-shaped nanopores. There may be two types of adsorbed I⁻ ions at the wedge-shaped nanopores: one is the weakly bonded I⁻ in the central region of the nanopores (Labeled as II in Fig. 7a). This type of I⁻ can be exposed to electrostatic attraction from either side of the wedge-shaped nanopores. As the large size and atomic weight and the low charge of I⁻, the one-side attraction is not enough to fix I⁻, and this kind of I⁻ is removable. Once the weakly bonded I⁻ inside the wedge-shaped nanopores move to the end of the wedge sites, they will be strongly bonded (the other kind of I⁻, Labeled I in Fig. 7a). This is because of the severe superposition of electric potentials from the charged walls of the narrowing nanopores at the end of the wedge site, resulting in a strong electrostatic attraction. In addition, it is well known that the properties of water in nanopores are different from those of bulk water (Levinger, 2002). In this study, the surface tension, density, and dielectric constant of water in the wedge-shaped nanopores could be expected to decrease significantly (Wang, 2014; Knight et al., 2018), because of the small size of the wedge-shaped nanopores

especially at the end of the wedge site. It is possible that changes in water properties could increase the propensity of I⁻ to lose its hydration sphere and form strong inner-sphere complexes with the surface of the wedge-shaped nanopore. However, some spectroscopic works (such as X-ray absorption spectroscopic) should be done in the future work to confirm this assumption. As for Chry-SNT, brucite and lizardite, although there are significant nanopores present in the samples (Fig. 4), all samples show low adsorption to I⁻ (Fig. 6a). This is because the nanopores are formed by the packing of nanotubes or particles in Chry-SNT, brucite and lizardite, this kind of nanopores may change when they are in solution, and they are not rigid pores. So the external surface adsorption is the major mechanism for chrysotile single nanotubes, brucite and lizardite (Fig. 7b), and this kind of adsorption is not strong enough to bond I⁻, due to iodide's large size and low charge. These results indicated the wedged-shaped nanopores in the chrysotile bundles, as well as the shape of nanopore geometry, are crucial in I⁻ adsorption process.

Nanopores are ubiquitous in natural environmental media including minerals, rocks, soils, sediments, and organism (Wang et al., 2003; Wang, 2014). It has become a consensus that nanopores play substantial roles in the treatment of environmental pollutants (Wang et al., 2002; Jung et al., 2012, 2016, 2019; Yu et al., 2015; Deng et al., 2017;

Wei et al., 2019) and other geosciences issues such as chemical weathering (Hochella and Banfield, 1995), element migration and enrichment (Cheng et al., 2012), and storage and transport of unconventional oil and gas (Bernard et al., 2012). For the first time, we found that chrysotile bundles with wedge-shaped nanopores exhibited a surprisingly large capacity of I^- adsorption and the pore shape of the adsorbent is a crucial parameter in I^- adsorption process. More attention should be paid to the role of pore shape regarding the immobilization or retardation of I^- as well as other anions. The current study also gives insight into the potential application of chrysotile on the adsorption of radioactive iodide in natural and engineered environments.

4. Conclusions

In this study, the adsorption of I^- from water by chrysotile was investigated for the first time. Chrysotile bundles (Chry-B) with wedge-shaped nanopores exhibited very strong adsorption to I^-, with a distribution coefficient (K_d) of 179.24 mL/g, which is two orders of magnitude higher than those for previously reported clay minerals (Miller et al., 2015). The adsorption isotherm of I^- fitted well with Langmuir isotherm and the Langmuir adsorption capacity of Chry-B was 4.13 mg/g, which is three orders of magnitude higher than those of natural soil samples (Dai et al., 2009) and one order of magnitude higher than that of ferrihydrite (Yu et al., 1996). The wedge-shaped nanopores among the neighboring nanotubes in Chry-B proved to be the primary adsorption sites for I^- by comparing the adsorption of Chry-B with those of dispersed chrysotile single nanotubes, lizardite and brucite. The severe superposition of electric potentials from the narrowing charged walls of the wedges constituted a key mechanism in I^- adsorption process, which significantly strengthened the electrostatic interaction between I^- and wedge surface > Mg-OH. These results demonstrated that the shape of nanopore geometry was crucial in I^- adsorption, and that chrysotile with significant reserves worldwide had the potential to be an inexpensive and efficient adsorbent for the radioactive iodide removal. What is more, this study also provided new insight to develop new anion adsorbents with wedge-shaped nanopores.

Declaration of Competing Interest

All the authors agree that there are no conflicts of interest to declare.

Acknowledgments

Appendix A. Supplementary data

Supplementary data to this article can be found online at https://doi.org/10.1016/j.clay.2019.105331.

References

Hydrous phyllosilicates (exclusive of micas). In: Bailey, S. (Ed.), Reviews in Mineralogy. vol. 19. Mineralogical Society of America, Washington, DC, pp. 725.

Bales, R.C., Morgan, J.J., 1985. Surface charge and adsorption properties of chrysotile asbestos in natural waters. Environ. Sci. Technol. 19, 1213–1219.

Baxter, G.P., Titus, A.C., 1940. A revision of the atomic weight of iodine. the ratio of silver iodide to silver chloride. J. Am. Chem. Soc. 62, 1826–1828.

Bernard, S., Wirth, R., Schreiber, A., Schulz, H.-M., Horsfield, B., 2012. Formation of nanoporous pyrobitumen residues during maturation of the barnett shale (Fort Worth Basin). Int. J. Coal Geol. 103, 3–11.

Brix, K., Hein, C., Haben, A., Kautenburger, R., 2019. Adsorption of caesium on raw Ca-bentonite in high saline solutions: influence of concentration, mineral composition, other radionuclides and modelling. Appl. Clay Sci. 182, 105275.

Cattaneo, A., Somigliana, A., Gemmi, M., Bernabeo, F., Savoca, D., Cavallo, D.M., Bertazzi, P.A., 2012. Airborne concentrations of chrysotile asbestos in serpentine quarries and stone processing facilities in Valmalenco. Italy. Ann. Occup. Hyg. 56, 671–683.

Chen, Y.Y., Yu, S.H., Yao, Q.Z., Fu, S.Q., Zhou, G.T., 2018. One-step synthesis of Ag2O@Mg(OH)2 nanocomposite as an efficient scavenger for iodine and uranium. J. Colloid Interface Sci. 510, 280–291.

Cheng, H., Hu, E., Hu, Y., 2012. Impact of mineral micropores on transport and fate of organic contaminants: a review. J. Contam. Hydrol. 129, 80–90.

Choung, S., Um, W., Kim, M., Kim, M.G., 2013. Uptake mechanism for iodine species to black carbon. Environ. Sci. Technol. 47, 10349–10355.

Couture, R.A., Seitz, M.G., 1983. Sorption of anions of iodine by iron oxides and kaolinite. Nucl. Chem. Waste Manage. 4, 301–306.

Dai, J.L., Zhang, M., Hu, Q.H., Huang, Y.Z., Wang, R.Q., Zhu, Y.G., 2009. Adsorption and desorption of iodine by various Chinese soils: II. Iodide and iodate. Geoderma 153, 130–135.

Decamp, C., Happel, S., 2013. Utilization of a mixed-bed column for the removal of iodine from radioactive process waste solutions. J. Radioanal. Nucl. Chem. 298, 763–767.

Deng, L.L., Yuan, P., Liu, D., Annabi-Bergaya, F., Zhou, J.M., Chen, F.R., Liu, Z.W., 2017. Effects of microstructure of clay minerals, montmorillonite, kaolinite and halloysite, on their benzene adsorption behaviors. Appl. Clay Sci. 143, 184–191.

Evarts, R.C., 1977. The geology and petrology of the del puerto ophiolite, Diablo Range, central California Coast Ranges. North American ophiolites: oreg. Dep. Geol. Miner. Ind. Bull. 95, 121–139.

Fuge, R., 2013. Soils and Iodine deficiency. In: Selinus, O. (Ed.), Essentials of Medical Geology: Revised Edition. Springer Netherlands, Dordrecht, pp. 417–432.

Gregg, S., Sing, K., SW, A., 1982. Surface area and Porosity. Academic Press Inc. Ltd., London, pp. 111–194.

Hayes, K.F., Roe, A.L., Brown, G.E., Hodgson, K.O., Leckie, J.O., Parks, G.A., 1987. In situ X-ray absorption study of surface complexes: Selenium oxyanions on α-FeOOH. Science 238, 783–786.

Hochella, M., Banfield, J., 1995. Chemical weathering of silicates in nature; a microscopic perspective with theoretical considerations. Rev. Mineral. Geochem. 31, 353–406.

Ikari, M., Matsui, Y., Suzuki, Y., Matsushita, T., Shirasaki, N., 2015. Removal of iodide from water by chlorination and subsequent adsorption on powdered activated carbon. Water Res. 68, 227–237.

Ji, S., Zhu, J., He, H., Tao, Q., Zhu, R., Ma, L., Chen, M., Li, S., Zhou, J., 2018. Conversion of serpentine to smectite under hydrothermal condition: implication for solid-state transformation. Am. Mineral. 103, 241–251.

Jung, H.B., Boyanov, M.I., Konishi, H., Sun, Y.B., Mishra, B., Kemner, K.M., Roden, E.E., Xu, H.F., 2012. Redox behavior of uranium at the nanoporous aluminum oxide-water interface: implications for uranium remediation. Environ. Sci. Technol. 46, 7301–7309.

Jung, H.B., Xu, H., Konishi, Roden, E.E., 2016. Role of nano-goethite in controlling U(VI) sorptin-desorption in subsurafce soil. J. Geochem. Explor. 169, 80–88.

Jung, H.B., Xu, H., Roden, E.E., 2019. Long-term sorption and desorption of uranium in sapolite subsoil with nanoporous goethite. Appl. Geochem. 102, 129–138.

Kaplan, D.I., Serne, R.J., Parker, K.E., Kutnyakov, I.V., 2000. Iodide sorption to subsurface sediments and Illitic minerals. Environ. Sci. Technol. 34, 399–405.

Kaplan, D.I., Denham, M.E., Zhang, S., Yeager, C., Xu, C., Schwehr, K., Li, H.-P., Ho, Y.-F., Wellman, D., Santschi, P.H., 2014. Radioiodine biogeochemistry and prevalence in groundwater. Crit. Rev. Environ. Sci. Technol. 44, 2287–2335.

Knight, A.W., Tigges, A.B., Ilgen, A.G., 2018. Adsorption of copper (II) on mesoporous silica: the effect of nano-scale confinement. Geochem. Trans. 19, 13.

Küpper, F.C., Carpenter, L.J., McFiggans, G.B., Palmer, C.J., Waite, T.J., Boneberg, E.-M., Woitsch, S., Weiller, M., Abela, R., Grolimund, D., 2008. Iodide accumulation provides kelp with an inorganic antioxidant impacting atmospheric chemistry. Proc. Nati. Acad. Sci. 105, 6954–6958.

Largitte, L., Pasquier, R., 2016. A review of the kinetics adsorption models and their application to the adsorption of lead by an activated carbon. Chem. Eng. Res. Des. 109, 495–504.

Levinger, N.E., 2002. Water in confinement. Science 298, 1722–1723.

Li, W., Beard, B.L., Li, C., Johnson, C.M., 2014. Magnesium isotope fractionation between brucite [Mg (OH) 2] and Mg aqueous species: implications for silicate weathering and biogeochemical processes. Earth Planet. Sci. Lett. 394, 82–93.

Limousin, G., Gaudet, J.-P., Charlet, L., Szenknect, S., Barthes, V., Krimissa, M., 2007. Sorption isotherms: a review on physical bases, modeling and measurement. Appl. Geochem. 22, 249–275.

Liu, D., Yuan, P., Tan, D.Y., Liu, H.M., Wang, T., Fan, M.D., Zhu, J.X., He, H.P., 2012. Facile preparation of hierarchically porous carbon using diatomite as both template and catalyst and methylene blue adsorption of carbon products. J. Colloid Interface Sci. 388, 176–184.

Liu, Y., Gu, P., Jia, L., Zhang, G., 2016. An investigation into the use of cuprous chloride for the removal of radioactive iodide from aqueous solutions. J. Hazard. Mater. 302, 82–89.

Martin, C.J., Phillips, V.A., 1977. The texture of chrysotile asbestos in relationship to mechanical properties. Mater. Sci. Eng. 30, 81–87.

Miller, A., Kruichak, J., Mills, M., Wang, Y., 2015. Iodide uptake by negatively charged clay interlayers? J. Environ. Radioact. 147, 108–114.

Morgan, A., 1997. Acid leaching studies of chrysotile asbestos from mines in the coalinga region of California and from Quebec and British Columbia. Ann. Occup. Hyg. 41, 249–268.

Muramatsu, Y., Uchida, S., Sriyotha, P., Sriyotha, K., 1990. Some considerations on the sorption and desorption phenomena of iodide and iodate on soid. Water Air Soil Pollut. 49, 125–138.

Mushtaq, S., Yun, S.-J., Yang, J.E., Jeong, S.-W., Shim, H.E., Choi, M.H., Park, S.H., Choi, Y.J., Jeon, J., 2017. Efficient and selective removal of radioactive iodine anions using engineered nanocomposite membranes. Environ. Sci. Nano 4, 2157–2163.

Naumann, A., Dresher, W., 1966. The morphology of chrysotile asbestos as inferred from nitrogen adsorption data. Am. Mineral. 51, 711–725.

Ohnishi, I., Nishioka, H., Okunishi, E., Takahashi, H., Kondo, Y., 2010. Cross-section of asbestos prepared for TEM/STEM with ion slicer. Microsc. Microanal. 16, 14–15.

Olson, B.G., Decker, J.J., Nazarenko, S., Yudin, V.E., Otaigbe, J.U., Korytkova, E.N., Gusarov, V.V., 2008. Aggregation of synthetic chrysotile nanotubes in the bulk and in solution probed by nitrogen adsorption and viscosity measurements. J. Phys. Chem. C 112, 12943–12950.

Pasbakhsh, P., Churchman, G.J., 2015. Natural Mineral Nanotubes: Properties and Applications. CRC Press, New York, pp. 131–140.

Pokrovsky, O.S., Schott, J., 2004. Experimental study of brucite dissolution and precipitation in aqueous solutions: surface speciation and chemical affinity control. Geochim. Cosmochim. Acta 68, 31–45.

Pundsack, F.L., 1961. The pore structure of chrysotile asbestos. J. Phys. Chem. 65, 30–33.

Pye, K., 1979. A review of asbestos substitute materials in industrial applications. J. Hazard. Mater. 3, 125–147.

Qian, Q., Shao, S., Yan, F., Yuan, G., 2008. Direct removal of trace ionic iodide from acetic acid via porous carbon spheres. J. Colloid Interface Sci. 328, 257–262.

Sazarashi, M., Ikeda, Y., Seki, R., Yoshikawa, H., 1994. Adsorption of I− ions on minerals for 129I waste management. J. Nucl. Sci. Technol. 31, 620–622.

Schoelwer, M.J., Zimmerman, D., Shore, R.M., Josefson, J.L., 2015. The use of 123I in diagnostic radioactive iodine scans in children with differentiated thyroid carcinoma. Thyroid 25, 935–941.

Sheppard, M.I., Thibault, D., McMurry, J., Smith, P., 1995. Factors affecting the soil sorption of iodine. Water Air Soil Pollut. 83, 51–67.

Sprynskyy, M., Niedojadło, J., Buszewski, B., 2011. Structural features of natural and acids modified chrysotile nanotubes. J. Phys. Chem. Solids 72, 1015–1026.

Stumm, W., 1992. The coordination chemistry of the hydrous oxide-water interface. In: Chemistry of the Solid-Water Interface. A Wiley-Interscience Publication, New York, pp. 13–27.

Ticknor, K., Cho, Y.-H., 1990. Interaction of iodide and iodate with granitic fracture-filling minerals. J. Radioanal. Nucl. Chem. 140, 75–90.

Ticknor, K., Vilks, P., Vandergraaf, T., 1996. The effect of fulvic acid on the sorption of actinides and fission products on granite and selected minerals. Appl. Geochem. 11, 555–565.

Turci, F., Colonna, M., Tomatis, M., Mantegna, S., Cravotto, G., Gulino, G., Aldieri, E., Ghigo, D., Fubini, B., 2012. Surface reactivity and cell responses to chrysotile asbestos nanofibers. Chem. Res. Toxicol. 25, 884–894.

Um, W., Serne, R.J., Krupka, K.M., 2004. Linearity and reversibility of iodide adsorption on sediments from hanford, Washington under water saturated conditions. Water Res. 38, 2009–2016.

Valentim, I.B., Joekes, I., 2006. Adsorption of sodium dodecylsulfate on chrysotile. Colloids Surf. A Physicochem. Eng. Asp. 290, 106–111.

Von Hippel, F.N., 2011. The radiological and psychological consequences of the fukushima daiichi accident. Bull. At. Sci. 67, 27–36.

Wang, Y., 2014. Nanogeochemistry: nanostructures, emergent properties and their control on geochemical reactions and mass transfers. Chem. Geol. 378–379, 1–23.

Wang, Y., Bryan, C., Xu, H., Pohl, P., Yang, Y., Brinker, C.J., 2002. Interface chemistry of nanostructured materials: ion adsorption on mesoporous alumina. J. Colloid Interface Sci. 254, 23–30.

Wang, Y., Bryan, C., Xu, H., Gao, H., 2003. Nanogeochemistry: geochemical reactions and mass transfers in nanopores. Geology 31, 387–390.

Wang, X., Chen, L., Wang, L., Fan, Q., Pan, D., Li, J., Chi, F., Xie, Y., Yu, S., Xiao, C., Luo, F., Wang, J., Wang, X., Chen, C., Wu, W., Shi, W., Wang, S., Wang, X., 2019a. Synthesis of novel nanomaterials and their application in efficient removal of radionuclides. Sci. China Chem. 62, 933–967.

Wang, Y., Huo, T., Feng, C., Zeng, Y., Yang, J., Zhang, X., Dong, F., Deng, J., 2019b. Chrysotile asbestos induces apoptosis via activation of the p53-regulated mitochondrial pathway mediated by ROS in A549 cells. Appl. Clay Sci. 182, 105245.

Wei, Y.F., Yuan, P., Liu, D., Losic, D.S., Tan, D.Y., Chen, F.R., Liu, H.C., Zhou, J.M., Du, P.X., Song, Y.R., 2019. Activation of natural halloysite nanotubes by introducing lanthanum oxycarbonate nanoparticles via co-calcination for outstanding phosphate removal. Chem. Commun. 55, 2110–2113.

Wicks, F., Plant, A., 1979. Electron-microprobe and X-ray microbeam studies of serpentine textures. Can. Mineral. 17, 785–830.

Yang, H., Xiao, Y., Liu, K., Yang, Y., Feng, Q., 2007. Physicochemical dispersion of chrysotile. Colloids Surf. A Physicochem. Eng. Asp. 301, 341–345.

Yang, D., Sarina, S., Zhu, H., Liu, H., Zheng, Z., Xie, M., Smith, S.V., Komarneni, S., 2011. Capture of radioactive cesium and iodide ions from water by using titanate nanofibers and nanotubes. Angew. Chem. 123, 10782–10786.

Yu, Z., Warner, J.A., Dahlgren, R.A., Casey, W.H., 1996. Reactivity of iodide in volcanic soils and noncrystalline soil constituents. Geochim. Cosmochim. Acta 60, 4945–4956.

Yu, W., Yuan, P., Liu, D., Deng, L., Yuan, W., Tao, B., Cheng, H., Chen, F., 2015. Facile preparation of hierarchically porous diatomite/MFI-type zeolite composites and their performance of benzene adsorption: the effects of NaOH etching pretreatment. J. Hazard. Mater. 173–181.

Yuan, P., Liu, D., Tan, D.-Y., Liu, K.-K., Yu, H.-G., Zhong, Y.-H., Yuan, A.-H., Yu, W.-B., He, H.-P., 2013. Surface silylation of mesoporous/macroporous diatomite (diatomaceous earth) and its function in Cu (II) adsorption: the effects of heating pretreatment. Microporous Mesoporous Mater. 170, 9–19.

Zhang, L., Jaroniec, M., 2017. SBA-15 templating synthesis of mesoporous bismuth oxide for selective removal of iodide. J. Colloid Interface Sci. 501, 248–255.